ChemNanoMat

CHEMNANOMAT
CHEMISTRY OF NANOMATERIALS FOR ENERGY, BIOLOGY AND MORE

ACES Asian Chemical Editorial Society

RESEARCH ARTICLE OPEN ACCESS

Engineered Self-Assembly of Plasmonic Gold Nanoparticles Into Two-Dimensional and Three-Dimensional Arrays Within the Pores of Porous Silicon Membranes

Juan J. Barrios-Capuchino[1] | Robbert Schuett[1] | Gerwin Chilla[1] | Patrick Huber[2,3] | Alexander Yu. Petrov[4,5] | Wolfgang J. Parak[1] | Florian Schulz[1]

[1]Fachbereich Physik, CHyN, Universität Hamburg, Hamburg, Germany | [2]Institute for Materials and X-ray Physics, Hamburg University of Technology, Hamburg, Germany | [3]Centre for X-ray and Nanoscience, Deutsches Elektronen-Synchrotron DESY, Hamburg, Germany | [4]Institute of Optical and Electronic Materials, Hamburg University of Technology, Hamburg, Germany | [5]Institute of Functional Materials for Sustainability, Helmholtz-Zentrum Hereon, Hamburg, Germany

Correspondence: Florian Schulz (florian.schulz@uni-hamburg.de)

Received: 2 October 2025 | **Revised:** 30 November 2025 | **Accepted:** 24 December 2025

Keywords: gold nanoparticles | nanofabrication | nanomaterials | porous silicon | surface-enhanced Raman spectroscopy

ABSTRACT

We report a facile centrifugation-based method for assembling polystyrene (PSSH)-functionalized gold nanoparticles (Au NPs) onto porous silicon (pSi) substrates in two distinct configurations: two- and three-dimensional (2D and 3D) assemblies. The 2D assemblies are densely packed monolayer coatings of the exposed Si-surfaces including the inner pore walls, whereas the 3D structures result from Au NPs clustering inside the pores. Remarkably, this shift from 2D to 3D architectures was achieved by minor modification of the PSSH coating thickness. Scanning electron microscopy (SEM) characterization confirmed the homogeneity and high packing density of these assemblies extending over several thousand square micrometers. This approach offers a straightforward and versatile route for the fabrication of well-ordered pSi–Au NP hybrid nanostructures with potential applications in catalysis, surface-enhanced spectroscopy and optical metamaterials.

1 | Introduction

pSi platforms have emerged as versatile host materials for incorporating plasmonic nanoparticles (NPs) into their porous networks. With their high porosity, large configurable surface area, and open matrix structure, pSi-based hybrids have attracted interest for applications in optics, catalysis, and sensing [1–6]. A method for precisely arranging plasmonic NPs as two-dimensional (2D) coatings or three-dimensional (3D) aggregates within pSi membranes could further expand their functionality and optimize their performance for such applications. Moreover, the precision and tunability of hierarchically pSi fabrication via metal-assisted catalytic etching (MACE) [7]—where metallic NPs serve as self-propelled etching centers within the pore structure—could be significantly enhanced through the controlled, well-defined arrangement of these NPs at the onset of the etching process.

Plasmonic NPs have unique optical and electric properties that depend strongly on their size, shape, and organization [8–12]. In particular, gold NPs (Au NPs) have been extensively studied as building blocks for 2D and 3D assemblies, owing to their syntheses being well developed, allowing for tunable individual and collective plasmonic resonances, and their chemical stability [11, 13–16]. However, despite promising efforts to incorporate plasmonic NPs into porous structures [2, 17–20], translating assemblies into uniform hybrid materials has proven difficult. Conventional in situ growth techniques, such as immersion/dipping plating [21, 22] and electrochemical deposition [23] often

lead to broad NP size distributions, uneven pore loading, and unwanted agglomeration at pore entrances [21, 24, 25]. These limitations hinder the reproducibility and uniformity required for functional devices.

An alternative strategy involves the ex situ incorporation of pre-synthesized colloidal NPs [26]. Advances in colloidal chemistry now allow precise control over NP size, shape, and surface chemistry [27], but incorporating them into porous substrates in a controlled and reproducible way remains a significant challenge. Achieving well-defined 2D and 3D NP arrangements within pSi requires a careful balance of NP–substrate, NP–NP, and NP–solvent interactions, as well as consideration of fluid dynamics during the assembly process.

Here, we present a robust and straightforward centrifugation-based method for fabricating pSi–AuNP hybrid platforms. By tuning NP size, ligand shell properties, and centrifugation parameters, we achieve either uniform 2D coatings of the inner pore walls or confined 3D aggregates extending into the pores. Our findings highlight the critical role of surface chemistry and fluid dynamics in directing assembly outcomes and demonstrate the potential of this approach for creating functional hybrid materials. This simple yet versatile strategy opens pathways to applications in the scalable fabrication of multiscale structured silicon, photonics, sensing, and catalysis.

2 | Experimental Section

2.1 | Materials

Macro-pSi membranes doped with phosphorus (n-type) were purchased from Smart Membranes GmbH (Germany). The membranes have a pore diameter of 1 µm and a pore pitch of 1.5 µm (MakroPorP1.5). The membranes were 5 mm × 5 mm in size and 0.05 mm in thickness. Tetrachloroauric(III) acid (≥99.9% trace metal basis), ascorbic acid (AA, ≥99.0%), sodium borohydride ($NaBH_4$, ≥98%), cetyltrimethylammonium bromide (CTAB, ≥ 98%), and cetyltrimethylammonium chloride (CTAC, ≥ 99%) were ordered from Merck/Sigma-Aldrich. Toluene (≥99.5%), tetrahydrofuran (≥99.5%), and ethanol (denat., 96%), were from VWR (USA). Thiolated polystyrenes (PSSH, 5kPSSH: M_n: 5300 g mol^{-1}, M_w = 5800 g mol^{-1}; 12kPSSH: M_n = 11,500 g mol^{-1}, M_w = 12,400 g mol^{-1}) were purchased from Polymer Source (Canada). Ultrapure water (18.6 MΩ cm, Millipore) was used for all experiments. All reagents were used without further treatments.

2.2 | Synthesis of Au NPs and Ligand Exchange

Au NPs with designated core diameters of d_c = 50 and 70 nm were synthesized according to the seeded growth protocol presented by Zheng et al. [28] with minor modifications and scaled up by a factor of 10 to achieve high Au NP concentrations as described previously [29]. Briefly, for the preparation of the initial CTAB-stabilized seeds, sodium borohydride ($NaBH_4$, 600 µL, 10 mM) was quickly added into a 10-mL mixture of CTAB (5 mL, 200 mM) and tetrachloroauric(III) acid ($HAuCl_4$, 5 mL, 0.5 mM) under rapid stirring (900 rpm). The final mixture remained undisturbed at room temperature for 3 h.

For the first growth step, aqueous solutions of AA (1.5 mL, 100 mM) and CTAC (2.0 mL, 200 mM) were mixed with 50 µL of the initial CTAB-coated seeds at 900 rpm, followed by addition of $HAuCl_4$ (2 mL, 0.5 mM). These synthesized Au NPs were stirred at 900 rpm for 15 min and then collected by centrifugation (21,000 g, 30 min). The pellet was dispersed in CTAC (1 mL, 20 mM), and these Au NPs were used as seeds for the growth of larger Au NPs. The AuNP concentration was estimated to be 21 nM by UV/vis spectroscopy using their absorbance at 450 nm as described by Haiss et al. [30] In their method, a theoretical analysis was experimentally confirmed by determining extinction coefficients for a range of spherical Au NP sizes, thereby allowing for the determination of Au NP size and concentration with UV/vis spectroscopy.

To synthesize Au NPs (50 nm), an aqueous solution of AA (1.3 mL, 10 mM) and CTAC (20 mL, 100 mM) was mixed with 150 µL of the Au NP seeds at 600 rpm and treated with ultrasound (Sonorex Super RK 103H, Bandelin) for 1 min, followed by a dropwise injection of $HAuCl_4$ (20 mL, 0.5 mM). The Au NPs were purified two times by centrifugation (9,000 g, 30 min), the first time the supernatant was replaced with water and the second time the pellet was redispersed in CTAC (1 mL, 20 mM) for the next growing step.

To synthesize Au NPs (70 nm), an aqueous solution of AA (1.3 mL, 10 mM) and CTAC (20 mL, 100 mM) was mixed with 300 µL of the previous Au NPs (Au NPs@50 nm) at 600 rpm and treated with ultrasound for 10 min, followed by a dropwise injection of $HAuCl_4$ (20 mL, 0.5 mM). The Au NPs were washed twice via centrifugation (5,000 g, 30 min) as described above and redispersed in CTAC (1 mL, 20 mM).

A direct ligand exchange of the Au NPs was performed based on the protocol presented by Schulz et al. [29]. The previously synthesized Au NPs were concentrated to a volume of ∼100 µL by centrifugation and removal of the supernatant. The redispersed pellet was then added dropwise to a solution of the according PSSH-ligand in tetrahydrofuran (THF, 6 mL, c(PSSH) = 1 mM) in a 100 ml single-neck round-bottom flaks under rapid stirring (600 rpm). The reaction was left stirring overnight. Then, the THF was removed under reduced pressure with a rotary evaporator, the dry residue was redispersed in 1 mL of toluene and purified by repeated centrifugation (four centrifugation steps, 7,000 g, 15 min, replacing 950 µl of the supernatant with toluene after each step). To ensure complete removal of CTAC, liquid–liquid phase extraction was performed. To this end, the Au NPs in toluene were added to a mixture of water and ethanol in a volume ratio 1:1:1. The mixture was shaken vigorously and after phase separation being completed, the ethanol/water phase was carefully removed with a pipette. This process was repeated four times. The final dispersion was washed three more times with toluene by centrifugation as described above. Finally, the Au NPs@PSSH were centrifuged (7,000 g, 15 min) and the pellet redispersed in 0.5 mL toluene.

2.3 | Standard Procedure for the Self-Assembly of Au NPs Within the Pores of Porous Silicon Membranes

The assembly of Au NPs@PSSH on the pSi membranes was performed by immersing pieces of the membranes (cut to sizes of ∼2.3 × 2.3 mm^2 with a glass cutter) in 20 µL of the according Au NP@PSSH dispersion in toluene in a 0.5 mL reaction tube. The pSi membranes were used without further treatment. The tube was carefully sealed

with parafilm to avoid evaporation of toluene, and the membranes were left in the dispersion for 24 h and then centrifuged. The substrates were placed at 45° to ensure the centrifugation force was perpendicular to the substrates' surfaces. The centrifugation parameters (ranging from 1,000 to 2,000 g and 30 to 60 min) and their impact on the outcome of the experiments are discussed in the main text. The pSi membranes were then removed from the dispersion and dried for 24 h at room temperature.

2.4 | Uv/Vis Spectroscopy

Absorbance measurements were carried out using a Cary Eclipse 60 spectrometer (Agilent). Quartz cuvettes (Hellma QS, Hellma, Germany) were used.

2.5 | Scanning Electron Microscopy

Scanning electron microscopy (SEM) micrographs were obtained using a Zeiss Sigma HD field emission SEM operated at an accelerating voltage of 10 kV. To characterize the distribution of the Au NPs on and in the pores of the pSi membranes, the impregnated substrates were directly deposited on a carbon tape. Cross-sectional images of the pSi-Au NP hybrids were performed by carefully cutting the membranes vertically with a glass cutter and depositing them directly on a carbon tape. High-resolution micrographs were obtained using an InLens detector with a working distance in the range of 2.6–3.2 mm.

Transmission electron microscopy (TEM) micrographs of Au NPs@PSSH were recorded with a JEOL JEM-1011 microscope with an operating voltage of 100 kV. The TEM samples were prepared by transferring Au NPs@PSSH that were self-assembled on a liquid subphase as described previously [29] onto a carbon-coated TEM grid. The Au NP core diameters d_c were obtained from the TEM micrographs using the software Image J 1.53e.

2.6 | Surface-Enhanced Raman Spectroscopy (SERS)

Raman spectroscopy was carried out using a Horiba LabRAM HR Evolution confocal micro spectrometer. The microscope is made by Olympus. A grating of 1800 gr/mm and a Syncerity 2D CCD detector were used. The confocal hole in front of the spectrometer was fully opened, allowing a conventional (nonconfocal) estimation of the sampling volume. A laser with 633 or 785 nm wavelength was used as light source. The laser was focused with a 100x plan objective onto the membrane surface with a spot diameter of ~1 μm in the range of the pore sizes. Spectra were recorded from 900 to 1200 cm^{-1} with a laser excitation power of 1600 μW on at least five different pores randomly distributed throughout each sample surface (Figure S7). In additional measurements, laser powers of 458 μW at 633 nm and 472 μW at 785 nm were used with a 10x (numerical aperture NA = 0.25) or a 100x objective (NA = 0.90) (Figures S8 and S9). The sampling volume was estimated as cylinder of width $w = 1.22\,\lambda/\mathrm{NA}$ and height $L = 4\,l/(\mathrm{NA})^2$. Integration time was 60 s, except for a PSSH plate control (450 μm thickness) where it was 6 s and the signal multiplied by 10 for comparisons. Intensities were evaluated relative to the according baselines. The baselines were corrected with asymmetric least square baseline correction. All experiments were performed at room temperature.

3 | Results

3.1 | Preparation and Structure of Au NP-Impregnated Porous Substrates

Scheme 1 illustrates the method to fabricate 2D and 3D arrays of Au NPs@PSSH on and within the pores of the pSi membranes. The Au NPs were functionalized with thiol-terminated PSSH ligands that stabilize the Au NPs and are known to facilitate their self-assembly into well-ordered thin-film supercrystals [29, 31–33]. First, we tested the self-assembly of Au NPs@PSSH with core diameters $d_c = 50$ and 70 nm, coated with two different ligands, 12kPSSH, and 5kPSSH, on diethylene glycol, which is an established protocol [29, 33–35]. TEM micrographs of the formed supercrystals are shown in Figure 1 confirming the uniformity and low dispersity of the Au NPs and their successful functionalization with the PSSH ligands. The interparticle spacing is affected by the molecular weight of the PSSH ligands, but not necessarily in a linear manner, as discussed in previous work [36]. No broadening of the plasmon resonance was observed in the absorbance spectra of the dispersed Au NPs@PSSH, confirming their colloidal stability (Figure S1). SEM micrographs of the commercially available pSi membranes show the rounded-square macropores arranged in a hexagonal structure with pore diameters of ~1 μm and a pore-to-pore distance (pitch) of 1.5 μm (Figure 1e).

To prepare hybrid structures, the pSi substrates were immersed in a dispersion containing the Au NPs@PSSH for 24 h. The use of toluene as solvent has shown promise in controlling and achieving large-scale self-assembly of Au NPs@PSSH into 2D and 3D supercrystals [29, 36]. In addition, it has been shown that toluene and 24 h of impregnation time help to fill and lead to a more homogenous deposition of Au NPs and FeCo NPs into the pores of pSi membranes [26, 37]. After this impregnation time, the dispersions with the immersed pSi membranes were centrifuged, which can enhance the infiltration of the Au NPs@PSSH into the pores. The self-assembly of Au NPs@PSSH on the surfaces or within the pores of the pSi membranes was tested for different combinations of Au NP core diameter and ligand size and for different centrifugation conditions (relative centrifugation force (RCF) and time (t_{cent})). The concentration of the according Au NPs@PSSH (50 or 70 nm) was kept constant for all experiments. The experiments with a clear outcome (optimized parameters) are summarized in Table 1.

After drying, the pSi–Au NPs@PSSH hybrid materials were studied with SEM. Three different sets of centrifugation parameters were tested: 1000 g for 60 min, 2000 g for 30 min, and 2000 g for 60 min. Figure 2 summarizes exemplary SEM micrographs with top views of the pSi membranes after their interaction with Au NPs (50 nm)@5kPSSH and Au NPs (70 nm)@12kPSSH under these different sets of centrifugation parameters. For the Au NPs (50 nm)@5kPSSH samples we observed that the surfaces of the pSi membranes were quite densely and homogeneously coated with monolayers, whereas the NP coverage at and around the pore peripheries was markedly reduced. This observation was consistent across different centrifugation conditions and suggests

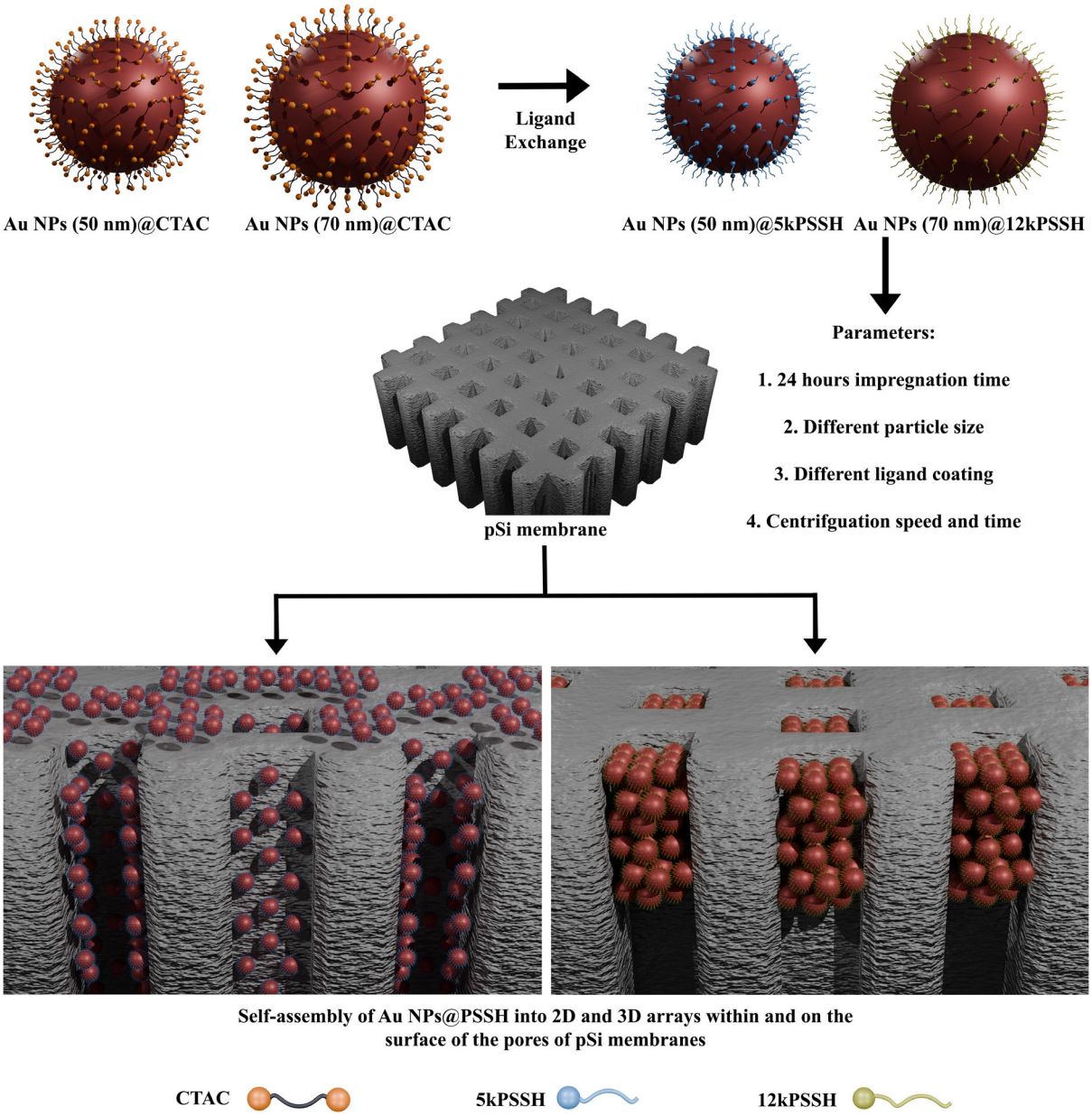

Self-assembly of Au NPs@PSSH into 2D and 3D arrays within and on the surface of the pores of pSi membranes

SCHEME 1 | Idealized schematic representation of the self-assembly of 2D and 3D arrays of Au NPs within and on the surface of the pores of pSi membranes. The Au NPs were functionalized with polystyrene (PSSH) ligand molecules, followed by their interaction with pSi under different parameters such as NP size, surface chemistry, centrifugation time, and speed.

that fluid dynamics near the pore entrances may play a role in modulating NP deposition. The homogeneity of the 2D coatings of the Au NPs (50 nm)@5kPSSH over large areas is shown in Figure S2. These 2D coatings can extend up to several thousand square micrometers. On the other hand, we observed completely different structures for Au NPs (70 nm)@12kPSSH after interacting with the pSi membranes under identical centrifugation conditions. Here, the pores were found to be partially or even completely filled with Au NPs (70 nm)@12kPSSH, while the top surfaces exhibited very low coverage, lacking monolayers and showing only occasional isolated NPs. For this 3D configuration, the areas with filled pores can also extend up to several thousand square micrometers (Figure S3) but smaller areas of several tens of square micrometers were more frequently observed. The degree of pore filling depended strongly on the centrifugation conditions. With 1,000 g the pores were only sparsely filled, with 30 min at 2,000 g most pores were completely filled and with 60 min at 2,000 g the pores were partially filled. In parallel to the reduced coverage observed at the pore peripheries for the smaller Au NPs (50 nm)@5kPSSH, the partial pore filling at longer centrifugation times for the larger Au NPs (70 nm)@12kPSSH may similarly reflect the influence of fluid dynamics during centrifugation on NP delivery and retention.

Cross-sectional SEM of the impregnated pSi membranes provided additional insights into the Au NPs' distribution within the pores (Figure 3). For Au NPs (50 nm)@5kPSSH, uniform coatings of the inner pore walls were observed, with no apparent gradient along the pore depth. This highlights the ability of the experimental conditions to promote homogeneous NP deposition within the confined geometry. For the Au NPs (70 nm)

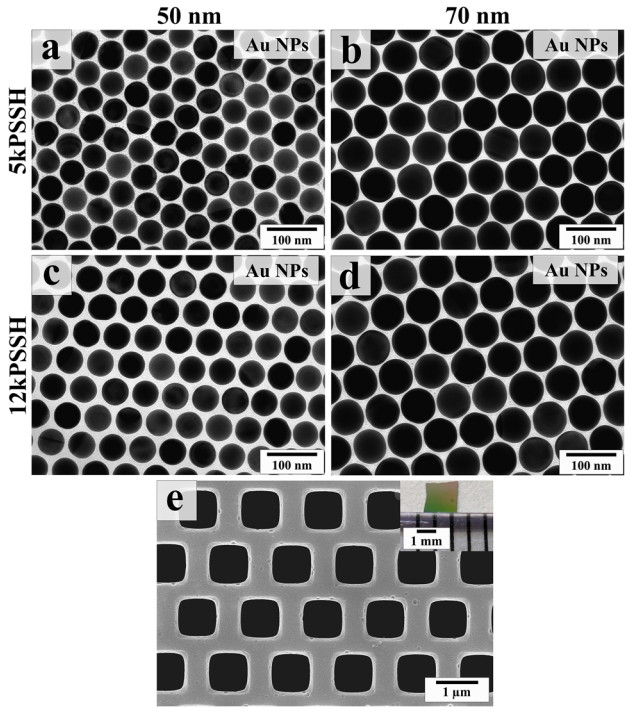

FIGURE 1 | (a–d) Transmission electron microscopy (TEM) images of Au NPs@PSSH monolayers obtained by self-assembly on a liquid subphase. The Au NP core diameters were 50 and 70 nm and the molecular weights of the PSSH ligands were ~5,000 Da (5kPSSH) and ~12,000 Da (12kPSSH) as indicated. (e) Scanning electron microscopy (SEM) micrograph of a pSi membrane. The inset shows a photograph of the ~2.3 × 2.3 mm^2 pSi membrane.

@12kPSSH under optimum pore-filling conditions (Figures 2d and 3d), cross-sectional SEM revealed that the pores were filled with compact aggregates extending approximately 1 µm into the pores. These structures appeared uniform in dimensions and density across the substrate, as confirmed by observations of multiple aggregates that detached upon membrane fracture (Figure S4). While they exhibited local close packing of NPs, no long-range order was evident. These results indicate that the pores can be filled in a defined and reproducible manner under optimized conditions, resulting in confined NP structures of high packing density.

To further clarify the role of ligand properties, we investigated Au NPs (50 nm)@12kPSSH and Au NPs (70 nm)@5kPSSH under identical centrifugation conditions (Figure S5). For Au NPs (50 nm)@12kPSSH, only sparse filling of the pores was observed, and no monolayers formed on the membrane surfaces or inner pore walls. In contrast, Au NPs (70 nm)@5kPSSH exhibited a behavior that was somehow similar to the 2D coatings found for Au NPs (50 nm)@5kPSSH, but with a stronger dependence on centrifugation conditions. At 1000 g, a uniform coating of the inner pore walls was achieved without deposition on the exposed surfaces (Figure S6). Increasing the force to 2000 g for 30 min resulted in dense 2D coatings on the membrane surfaces (again with reduced coverage at the pore peripheries), while prolonged centrifugation at 2000 g for 60 min led to partial removal of these coatings, indicating a "washing" effect. Notably, no complete pore clogging was observed for either configuration, underlining the strong impact and delicate interplay of NP size and ligand length on the assembly behavior within and on the porous membranes. The experiments were repeated at least three times and the results were reproducible when the experiments were repeated using different batches of Au NPs@PSSH.

3.2 | Raman Measurements

Raman measurements performed on the hybrid structures formed by Au NPs (50 nm)@5kPSSH (2D) and Au NPs (70 nm)@12kPSSH (3D) under optimum conditions (cf. Figure 2c,d) confirmed the presence of PSSH ligands and showed little variations in signal intensities across different spots, indicating structural homogeneity (Figure S7). The Raman signals from both hybrid configurations were comparable in intensity, suggesting that both arrangements are capable of providing sufficient plasmonic enhancement for ligand detection. To obtain a rough estimate of the enhancement, a polystyrene plate (450 µm thickness, PS plate) was measured for comparison. A comparison of 633 and 785 nm excitation was also done on an Au NPs (70 nm)@12kPSSH/pSi hybrid structure. In optical microscopy the filled pores appear golden, but coated and incompletely filled pores appear black and cannot be distinguished from empty ones (Figure S7). With a 100x objective, the laser spot size of ~1 µm was similar to the pore size and single pores could be measured. Based on the geometry of the aggregates in the clogged pores, the number of Au NPs was roughly estimated to be ~1000 per clogged pore. Based on previous work, the grafting density of the 12kPSSH ligands can be estimated to be 0.5 nm^{-2} [36]. With an estimate of the focal volume in the PS plate (Methods) the intensity could then be normalized with the number of PSSH monomers, additional to a normalization with laser power density. The results are summarized in Figure 4. The spectra are provided as Supporting Information (Figures S8 and S9). This approach gives a very conservative and rough estimate of the effective enhancement factor (Figure 4a). The enhancement factors determined by this approach are very low: ~19 for 785 nm and just 1.7 for 633 nm. The reasons are that only small volumes of the

TABLE 1 | Optimized parameters used for the self-assembly of Au NPs@PSSH on porous silicon membranes: Dimensionality of the array, immersion time t_{immers}, NP concentrations c_{NP}, and centrifugation parameters (relative centrifugal force, RCF, and centrifugation time t_{cent}). All samples were prepared at room temperature.

Sample	Array dimension	t_{immers}, h	c_{NP}, nM	RCF	t_{cent}, min
Au NPs (50 nm)@5kPSSH	2D	24	~2.2	2,000	30
				1,000	60
Au NPs (70 nm)@5kPSSH	2D	24	~ 1.1	1,000	60
Au NPs (70 nm)@12kPSSH	3D	24	~ 1.1	2,000	30

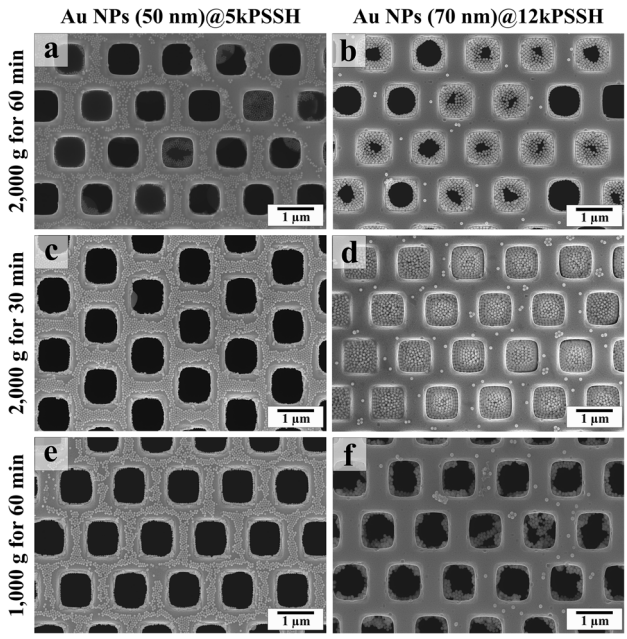

FIGURE 2 | SEM images of porous silicon (pSi) membranes after interaction with PSSH-functionalized Au NPs. Top view of pSi membranes after interacting with Au NPs (50 nm)@5kPSSH and Au NPs (70 nm)@12kPSSH under different centrifugation parameters as indicated.

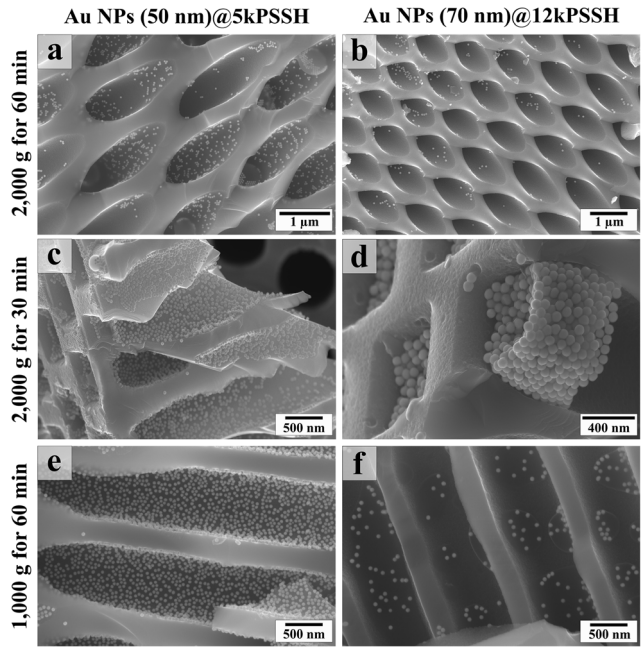

FIGURE 3 | Cross-sectional view of the porous membranes after interacting with Au NPs (50 nm)@5kPSSH and Au NPs (70 nm)@12kPSSH under different centrifugation parameters. The samples shown are the same as in Figure 2 but with a cross-sectional (tilted) view that reveals the structures inside the pores.

samples are "hot spots" with a high local enhancement of the electromagnetic field and that the light field is distributed among many hot spots and absorbers [38]. By analyzing hot spots alone, a much larger enhancement factor would result [29], but we limit our discussion here to the effective enhancement factor averaged over all molecules, not only those in hot spots. Another reason for the low enhancement factors is plasmonic losses. Au NPs are very good absorbers and this absorption necessarily reduces the measured intensity of Raman scattered light [39]. Accordingly, for the filled pores, not all Au NPs will be sampled, but only the top layers.

This is consistent with the observation, that the signal intensities where not strongly reduced on "black" pores with much less Au NPs (Figure 4b). It is impossible to quantify the amount of Au NPs in these pores based on optical microscopy, but based on the SEM analysis, the number is markedly reduced. Another important finding is that excitation dependence scales very differently for the PS plate control and the plasmonic porous structures. For the PS plate, the intensity ratios of 633 nm excitation to 785 nm excitation (I(633 nm)/I(785 nm)) are much higher (Figure S10). This underlines the plasmonic contributions in the hybrid structures. In plasmonic structures, the field enhancement does not track the absorption but is redshifted spectrally which is known as near-field-far-field shift [40, 41]. In consequence, the spectral region for optimum Raman enhancement/intensity is significantly shifted from 633 nm toward 785 nm. This is an interesting region for sensing applications, because in general background scattering, absorption and autofluorescence are reduced. It is also worth noting that due to the different scaling (with volume for the PS plates and with area for the plasmonic Au NPs/pSi hybrid structures) and plasmonic near-field enhancement effects, the intensities (without normalization) are higher when measuring with a 10x objective compared to a 100x objective for the PS plates, whereas the opposite is the case for the Au NPs/pSi hybrid structures (Figures S8 and S9). In the context of surface-enhanced Raman spectroscopy (SERS) it can be concluded that the 2D surface-assembled structures (as in Figure 2c) are favorable and the pore-filled structures (Figure 2d) bring no advantage in terms of enhancement due to competing plasmonic losses.

4 | Discussion of Au NP–Pore Interactions

The main observations of the experiments—which were reproducible for different batches of AuNP@PSSH—are two distinct structural outcomes: surface-assembled (2D) versus pore-filling (3D) for the different Au NP@PSSH samples tested. Additionally, we found a clear effect of centrifugation parameters. Of note, without centrifugation—when the pSi was simply immersed in the Au NP@PSSH dispersions for 24 h—we observed neither 2D nor 3D assemblies. For the shorter ligand 5kPSSH surface-assembled structures were observed for both Au NP core sizes (50 and 70 nm), however with different dependencies on centrifugation parameters. For the longer ligand 12kPSSH complete pore-filling was only observed for the larger Au NP (70 nm) under optimum centrifugation conditions. Additional key observations were the reduced coverages at pore peripheries and the dependence on centrifugation parameters in general.

These observations point at several key contributions in the assembly experiments:

1. Fluid mechanics which are governed by centrifugation parameters. These govern the interplay of Au NP@PSSH delivery, pore infiltration, retention, and hydrodynamic shear, which could, for instance, explain the reduced coverage at pore peripheries.

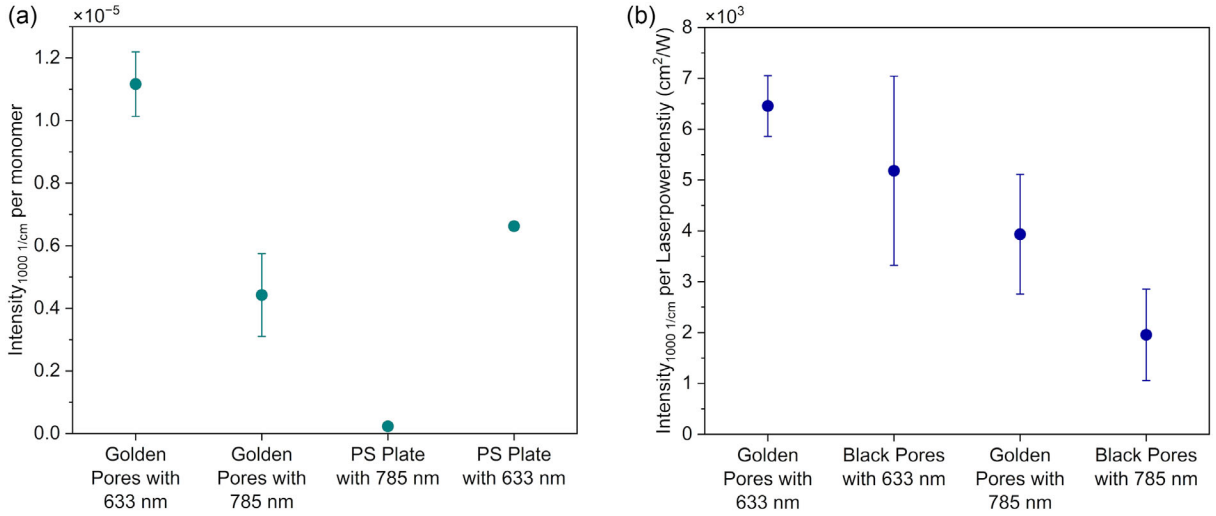

FIGURE 4 | Results of Raman measurements on impregnated pSi substrates. (a) Mean intensity at 1000 cm^{-1} measured on golden pores and on a polystyrene plate with 633 or 785 nm laser excitation. The intensities are normalized with the power of the exciting lasers and the estimated numbers of monomers. (b) Mean intensity at 1000 cm^{-1} measured on golden and black (i.e., less filled) pores on a pSi- Au NPs (70 nm)@12kPSSH sample with 633 or 785 nm laser excitation. The intensities are normalized with the power density of the exciting laser.

2. Au NP@PSSH–substrate interactions, which are modulated by the thickness of the ligand coating which in turn is modulated by centrifugation parameters leading to compression upon contact with the substrate. The thickness of a 5kPSSH coating in toluene dispersion was determined to be ~5 nm and that of a 12kPSSH coating as ~8 nm in previous work [36, 42]. Comparison of the attractive van der Waals interactions between bare AuNP–AuNP (no coating) and bare AuNP–Si surfaces shows that the AuNP–Si surface interaction is consistently stronger, regardless of the separation distance (Figure S11). These attractive interactions are reduced by both: solvent screening effects and the ligand coatings which increase the separation distance Au NP core–substrate and add a repulsive interaction. Accordingly, the longer ligand PSSH12k leads to a reduced adhesion. A detailed discussion is provided as Supporting Information (Note 1 and Figure S12). Additional noncovalent attractive ligand–substrate interactions might also contribute.

3. Au NP@PSSH–Au NP@PSSH and Au NP@PSSH–solvent interactions. Toluene is a good solvent for the PSSH-based PSSH ligands and accordingly in toluene, the Au NPs@PSSH are well-dispersed and colloidally stable. As the toluene evaporates during drying, the ligand shells transition from a swollen to a collapsed state, making ligand–ligand interactions attractive and promoting Au NPs@PSSH interparticle aggregation. This is commonly exploited in self-assembly of PSSH-coated NPs with multiple examples in literature [31, 43, 44].

With these contributions in mind, the experimental outcomes can be rationalized. In the case of 5kPSSH coatings, the Au NPs@5kPSSH–substrate interactions are sufficiently strong under optimized centrifugation conditions to result in densely packed monolayer coatings (2D) of the exposed surfaces and the inner pore walls. The Au NPs@5kPSSH mass affects the resulting compression of the ligand shell upon contact with Si-surfaces under a given RCF, but also changes their inertia which in turn dictates how they are affected by hydrodynamic shear. This might explain why the different Au NP sizes, Au NPs (50 nm)@5kPSSH and Au NPs (70 nm)@5kPSSH, are differently affected by the centrifugation parameters. Under optimized centrifugation conditions, a dense and homogeneous coating of the inner pore walls could be achieved for both AuNP sizes. If the centrifugation time, t_{cent}, was too long, the coverage was reduced, indicating that shear forces overcame adhesion, leading to a "washing" effect. Overall, the combination of strong NP–substrate adhesion and manageable shear forces under optimized centrifugation conditions explains why 5kPSSH systems consistently lead to 2D monolayer assembly (inside the pores, on the substrate, or both) rather than 3D clogging.

For 12kPSSH coated Au NPs, the overall outcome shifts from 2D coating to 3D pore clogging. The following factors contribute to this behavior. In the case of the 12kPSSH coatings, the NP-substrate adhesion is significantly reduced, while attractive ligand–ligand interactions upon solvent evaporation are increased. In consequence interparticle interactions are favored over surface adhesion leading to cluster formation. For the bigger Au NPs (70 nm)@12kPSSH, a larger overlap area with more ligand–ligand interactions increases the chance of cluster nucleation and growth. We speculate that drying effects may also contribute. When the pSi substrates dry after impregnation with the Au NP@PSSH dispersions, the toluene on exposed surfaces evaporates much faster than in the filled pores. Capillary effects might then lead to the observed uniform clogging behavior with densely packed 3D aggregates extending about 1 µm into the pores. Although the flow of the dispersion was not measured directly in situ, the presence of menisci (Figure 3d) and uniform radial growth of pore-filling aggregates (Figure 2b) are consistent with a capillary-driven retention and localized drying effects. This mechanism should therefore be considered a supported hypothesis rather than an experimentally directly confirmed process. For the smaller Au NPs (50 nm)@12kPSSH, the interparticle

interactions are less attractive due to less ligand–ligand contacts and the volume is smaller. Both might contribute to the less efficient clogging that was observed. However, it might be possible to achieve complete pore filling for smaller Au NPs by further optimizing centrifugation parameters and increasing particle concentrations. Taken together, reduced surface adhesion and increased ligand–ligand interactions for the thicker 12kPSSH coatings shift the balance toward interparticle aggregation, explaining why these systems favor 3D pore filling over 2D surface assemblies.

5 | Conclusion

In summary, we have developed a straightforward method, where PSSH-functionalized Au NPs and centrifugal force are implemented to tune the 2D and 3D self-assembly of Au NPs on the surfaces and in the pores of pSi membranes. Under optimized parameters high-density coatings of the inner pore walls can be achieved. Remarkably, a slight difference in coating thickness by changing the molecular weight of the coating ligand leads to a completely different outcome of the impregnation experiments. This behavior can be rationalized with the balance of NP–NP versus NP–substrate interactions in interplay with the fluid dynamics tuned by centrifugation parameters and upon drying. Since pSi membranes are commercially available and NP syntheses, including their functionalization with PSSH-based ligands, are well-established, the method can easily be implemented to explore further design parameters of both, porous substrates (material, pore size, pitch, and hierarchical pores) and NPs (material, size, and shape). While we focused here on the synthesis procedure and possible explanations for the observed outcomes, we envision several potential directions and applications that could be explored in future work.

The ability to obtain either uniform 2D coatings or confined 3D aggregates within porous substrates through adjusting NP and process parameters offers new opportunities for functional hybrid materials. For instance, the high-density inner pore coatings could serve as catalytic surfaces or as SERS-active interfaces for analyte detection in flow-through systems. The 3D aggregates, on the other hand, may be exploited as confined plasmonic domains potentially enabling optical sensing applications. Combining such structures with microfluidic systems could provide further control over mass transport and enable studies of dynamic processes under flow conditions. In this context it will also be interesting to explore if more complex ligand layer compositions can be incorporated, for instance towards biosensing applications. Moreover, the use of pore arrays as templates for assembling NPs into plasmonic supercrystals might open new directions in optical metamaterials, where coupled photonic and plasmonic modes could be explored [6, 45]. While these ideas remain speculative at this stage, they underline the broader potential of the straightforward method presented here as a platform for designing functional hybrid materials with tailored nanostructures. Open challenges and questions towards applications include scalability and stability of these hybrid structures, for instance under harsh catalytic conditions. In summary, the simplicity and versatility of this approach provide a promising platform for the design of functional hybrid materials with tunable nanoscale architectures.

Author Contributions

Juan J. Barrios-Capuchino: investigation (lead), visualization (lead), writing – original draft (equal), writing – review & editing (equal). **Robbert Schuett:** formal analysis (equal), investigation (equal), methodology (supporting), validation (equal), visualization (equal), writing – review & editing (supporting). **Gerwin Chilla:** formal analysis (equal), investigation (supporting), methodology (equal), visualization (supporting), writing – review & editing (supporting). **Patrick Huber:** conceptualization (equal), resources (equal) supervision (equal), writing – original draft (equal), writing – review & editing (equal). **Alexander Yu. Petrov:** conceptualization (equal), supervision (equal), writing – original draft (equal), writing – review & editing (equal). **Wolfgang J. Parak:** conceptualization (equal), resources (lead), supervision (equal), writing – original draft (equal), writing – review & editing (equal). **Florian Schulz:** conceptualization (lead), investigation (supporting), supervision (lead), visualization (supporting), writing – original draft (equal), writing – review & editing (equal).

Acknowledgments

This work was funded by the Deutsche Forschungsgemeinschaft (DFG, German Research Foundation) as part of the Excellence Strategy of the Federal Government and the federal states – EXC 3120/1 BlueMat: Water-Driven Materials - 533771286. J.J.B.C. gratefully acknowledges the Mexican National Council for Science and Technology (CONACYT) for his doctoral scholarship no. 862535. The Raman measurements were supported by the DFG under the project: 515366497.

Open Access funding enabled and organized by Projekt DEAL.

Conflicts of Interest

The authors declare no conflicts of interest.

Data Availability Statement

The data that support the findings of this study are available from the corresponding author upon reasonable request.

References

1. H. V. Bandarenka, K. V. Girel, S. A. Zavatski, A. Panarin, and S. N. Terekhov, "Progress in the Development of SERS-Active Substrates Based on Metal-Coated Porous Silicon," *Materials* 11, no. 5 (2018): 852.

2. P. Granitzer and K. Rumpf, "Porous Silicon—A Versatile Host Material," *Materials* 3, no. 2 (2010): 943–998.

3. S. Arshavsky-Graham, N. Massad-Ivanir, E. Segal, and S. Weiss, "Porous Silicon-Based Photonic Biosensors: Current Status and Emerging Applications," *Analytical Chemistry* 91, no. 1 (2019): 441–467.

4. D. I. Potemkin, D. K. Maslov, K. Loponov, et al., "Porous Nanocrystalline Silicon Supported Bimetallic Pd-Au Catalysts: Preparation, Characterization, and Direct Hydrogen Peroxide Synthesis.," *Frontiers in Chemistry* 6 (2018): 85.

5. S. Mariani, A. Paghi, A. A. La Mattina, A. Debrassi, L. Dähne, and G. Barillaro, "Decoration of Porous Silicon with Gold Nanoparticles via Layer-by-Layer Nanoassembly for Interferometric and Hybrid Photonic/Plasmonic (Bio)sensing," *Acs Applied Materials & Interfaces* 11, no. 46 (2019): 43731–43740.

6. R. F. Balderas-Valadez, R. Schürmann, and C. Pacholski, "One Spot—Two Sensors: Porous Silicon Interferometers in Combination With Gold Nanostructures Showing Localized Surface Plasmon Resonance," *Frontiers in Chemistry* 7 (2019):593.

7. S. Gries, M. Brinker, B. Zeller-Plumhoff, et al., "Wafer-Scale Fabrication of Hierarchically Porous Silicon and Silica by Active

Nanoparticle-Assisted Chemical Etching and Pseudomorphic Thermal Oxidation," *Small* 19, no. 22 (2023): 2206842.

8. K. L. Kelly, E. Coronado, L. L. Zhao, and G. C. Schatz, "The Optical Properties of Metal Nanoparticles: The Influence of Size, Shape, and Dielectric Environment," *Journal of Physical Chemistry B* 107 (2003): 668.

9. D. J.d Aberasturi, A. B. Serrano-Montes, and L. M. Liz-Marzán, "Modern Applications of Plasmonic Nanoparticles: From Energy to Health," *Advanced Optical Materials* 3 (2015): 602.

10. W. J. Wang, M. Ramezani, A. I. Väkeväinen, P. Törmä, J. G. Rivas, and T. W. Odom, "The Rich Photonic World of Plasmonic Nanoparticle Arrays," *Materials Today* 21, no. 3 (2018): 303–314.

11. A. Klinkova, R. M. Choueiri, and E. Kumacheva, "Self-Assembled Plasmonic Nanostructures," *Chemical Society Reviews* 43, no. 11 (2014): 3976.

12. Y.-Y. Cai, Y. C. Choi, and C. R. Kagan, "Chemical and Physical Properties of Photonic Noble-Metal Nanomaterials," *Advanced Materials* 35, no. 34 (2023): 2108104.

13. R. Borah, A. G. K.R., A. C. Minja, and S. W. Verbruggen, "A Review on Self-Assembly of Colloidal Nanoparticles into Clusters, Patterns, and Films: Emerging Synthesis Techniques and Applications," *Small Methods* 7, no. 6 (2023): 2201536.

14. Y. Yang, S. Matsubara, M. Nogami, J. Shi, and W. Huang, "One-Dimensional Self-Assembly of Gold Nanoparticles for Tunable Surface Plasmon Resonance Properties," *Nanotechnology* 17, no. 11 (2006): 2821.

15. D. García-Lojo, S. Núñez-Sánchez, S. Gómez-Graña, et al., Plasmonic Supercrystals," *Accounts of Chemical Research* 52, no. 7 (2019): 1855–1864.

16. C. Hamon, S. M. Novikov, L. Scarabelli, et al., "Collective Plasmonic Properties in Few-Layer Gold Nanorod Supercrystals," *ACS Photonics* 2, no. 10 (2015): 1482–1488.

17. M. L. Chourou, K. Fukami, T. Sakka, and Y. H. Ogata, "Gold Electrodeposition into Porous Silicon: Comparison between Meso- and Macroporous Silicon," *Physica Status Solidi C* 8, no. 6 (2011): 1783–1786.

18. L. Santinacci, T. Djenizian, P. Schwaller, T. Suter, A. Etcheberry, and P. Schmuki, "Selective Electrochemical Gold Deposition onto p-Si (1 0 0) Surfaces," *Journal of Physics D: Applied Physics* 41, no. 17 (2008): 175301.

19. S. N. Agafilushkina, O. Žukovskaja, S. A. Dyakov, et al., "Raman Signal Enhancement Tunable by Gold-Covered Porous Silicon Films with Different Morphology," *Sensors* 20, no. 19 (2020): 5634.

20. H. Li, Q. Wang, N. Gao, et al., "Facile Synthesis of Magnetic Ionic Liquids/Gold Nanoparticles/Porous Silicon Composite SERS Substrate for Ultra-Sensitive Detection of Arsenic," *Applied Surface Science* 545 (2021): 148992.

21. A. M. Alwan, I. A. Naseef, and A. B. Dheyab, "Well Controlling of Plasmonic Features of Gold Nanoparticles on Macro Porous Silicon Substrate by HF Acid Concentration," *Plasmonics* 13, no. 6 (2018): 2037–2045.

22. I. H. Hadi, D. Sulaiman, A. A. Jabbar, and A. M. Alwan, "Develop Synthesis and Characterization of Dual-Faced Porous Silicon/Gold Nanoparticle Hybrid Structures," *Silicon* 16 (2024): 4763–4771.

23. K. Fukami, Porous Silicon and Electrochemical Deposition, In: *In Handbook of Porous Silicon*, L. Canham, Springer International Publishing: Cham, 2017, pp. 1–10.

24. L. A. Wali, K. K. Hasan, and A. M. Alwan, "An Investigation of Efficient Detection of Ultra-Low Concentration of Penicillins in Milk Using AuNPs/PSi Hybrid Structure," *Plasmonics* 15, no. 4 (2020): 985–993.

25. L. A. Wali, K. K. Hasan, and A. M. Alwan, "Rapid and Highly Efficient Detection of Ultra-Low Concentration of Penicillin G by Gold Nanoparticles/Porous Silicon SERS Active Substrate," *Spectrochimica Acta Part A: Molecular and Biomolecular Spectroscopy* 206 (2019): 31–36.

26. M. B. de la Mora, J. Bornacelli, R. Nava, R. Zanella, and J. A. Reyes-Esqueda, "Porous Silicon Photoluminescence Modification by Colloidal Gold Nanoparticles: Plasmonic, Surface and Porosity Roles," *Journal of Luminescence* 146 (2014): 247–255.

27. Y. Xia, K. D. Gilroy, H.-C. Peng, and X. Xia, "Seed-Mediated Growth of Colloidal Metal Nanocrystals," *Angewandte Chemie International Edition* 56, no. 1 (2017): 60–95.

28. Y. Zheng, X. Zhong, Z. Li, and Y. Xia, Successive, Seed-Mediated Growth for the Synthesis of Single-Crystal Gold Nanospheres with Uniform Diameters Controlled in the Range of 5-150 nm," *Particle & Particle Systems Characterization* 31, no. 2 (2014): 266–273.

29. F. Schulz, O. Pavelka, F. Lehmkühler, et al., "Structural Order in Plasmonic Superlattices," *Nature Communications* 11, no. 1 (2020): 3821.

30. W. Haiss, N. T. K. Thanh, J. Aveyard, and D. G. Fernig, "Determination of Size and Concentration of Gold Nanoparticles from UV-Vis Spectra," *Analytical Chemistry* 79 (2007): 4215.

31. K. J. Si, Y. Chen, Q. Shi, and W. Cheng, "Nanoparticle Superlattices: The Roles of Soft Ligands," *Advancement of Science* 5, no. 1 (2018): 1700179.

32. X. W. Gu, X. Ye, D. M. Koshy, S. Vachhani, P. Hosemann, and A. P. Alivisatos, "Tolerance to Structural Disorder and Tunable Mechanical Behavior in Self-Assembled Superlattices of Polymer-Grafted Nanocrystals," *Proceedings of the National Academy of Sciences of the United States of America* 114, no. 11 (2017): 2836.

33. X. C. Ye, C. H. Zhu, P. Ercius, et al., "Structural Diversity in Binary Superlattices Self-Assembled from Polymer-Grafted Nanocrystals," *Nature Communications* 6 (2015): 10052.

34. A. Dong, J. Chen, P. M. Vora, J. M. Kikkawa, and C. B. Murray, "Binary Nanocrystal Superlattice Membranes Self-Assembled at the Liquid–Air Interface," *Nature* 466, no. 7305 (2010): 474.

35. E. V. Shevchenko, D. V. Talapin, N. A. Kotov, S. O'Brien, and C. B. Murray, "Structural Diversity in Binary Nanoparticle Superlattices," *Nature* 439, no. 7072 (2006): 55–59.

36. F. Schulz and H. Lange, "Optimizing Interparticle Gaps in Large-Scale Gold Nanoparticle Supercrystals for Flexible Light-Matter Coupling," *Advanced Optical Materials* 10, no. 24 (2022): 2202064.

37. M. Lepesant, B. Bardet, L.-M. Lacroix, et al., "Impregnation of High-Magnetization FeCo Nanoparticles in Mesoporous Silicon: An Experimental Approach," *Frontiers in Chemistry* 6, (2018): 609.

38. N. S. Mueller, E. Pfitzner, Y. Okamura, et al., "Surface-Enhanced Raman Scattering and Surface-Enhanced Infrared Absorption by Plasmon Polaritons in Three-Dimensional Nanoparticle Supercrystals," *ACS Nano* 15, no. 3 (2021): 5523–5533.

39. T. van Dijk, S. T. Sivapalan, B. M. DeVetter, et al., "Competition Between Extinction and Enhancement in Surface-Enhanced Raman Spectroscopy," *Journal of Physical Chemistry Letters* 4, no. 7 (2013): 1193–1196.

40. J. Zuloaga and P. Nordlander, "On the Energy Shift between Near-Field and Far-Field Peak Intensities in Localized Plasmon Systems," *Nano Letters* 11 (2011): 1280.

41. M. Rodio, M. Graf, F. Schulz, N. S. Mueller, M. Eich, and H. Lange, "Experimental Evidence for Nonthermal Contributions to Plasmon-Enhanced Electrochemical Oxidation Reactions," *ACS Catalysis* 10, no. 3 (2020): 2345–2353.

42. F. Schulz, S. Tober, and H. Lange, "Size-Dependent Phase Transfer Functionalization of Gold Nanoparticles To Promote Well-Ordered Self-Assembly," *Langmuir* 33, no. 50 (2017): 14437–14444.

43. F. Schulz, I. Lokteva, W. J. Parak, and F. Lehmkühler, "Recent Notable Approaches to Study Self-Assembly of Nanoparticles with X-Ray Scattering and Electron Microscopy," *Particle & Particle Systems Characterization* 38, no. 9 (2021): 2100087.

44. C. Yi, Y. Yang, B. Liu, J. He, and Z. Nie, "Polymer-Guided Assembly of Inorganic Nanoparticles," *Chemical Society Reviews* 49, no. 2 (2020): 465–508.

45. R. F. Balderas-Valadez and C. Pacholski, "Plasmonic Nanohole Arrays on Top of Porous Silicon Sensors: A Win–WIn Situation," *Acs Applied Materials & Interfaces* 13, no. 30 (2021): 36436–36444.

Supporting Information

Additional supporting information can be found online in the Supporting Information section. **Supporting Fig. S1:** Normalized absorbance spectra of AuNPs (50 nm and 70 nm) functionalized with 5KPSSH (dark and blue) and with 12KPSSH (red and yellow) in toluene. **Supporting Fig. S2:** Top view scanning electron microscopy (SEM) images of porous silicon membranes after interaction with Au NPs (50 nm)@5kPSSH under different centrifugation parameters. **Supporting Fig. S3:** Top view scanning electron microscopy (SEM) images of porous silicon membranes after interaction with Au NPs (70 nm)@12kPSSH. **Supporting Fig. S4:** Top view SEM images of self-assembled Au NPs (70 nm)@12kPSSH with similar pore shapes of the pores of pSi membranes, randomly dispersed on the carbon tape. These experiments were performed with the following centrifugation parameter: 2,000 g for 30 min. **Supporting Fig. S5:** Top view scanning electron microscopy (SEM) images of porous silicon membranes after interaction with Au NPs (50 nm)@12kPSSH and Au NPs (70 nm)@5kPSSH under different centrifugation parameters. **Supporting Fig. S6:** SEM images of pSi after interaction with Au NPs (70 nm)@5kPSSH. Top view and crosssection SEM images of pSi after interacting with Au NPs (70 nm)@5kPSSH under centrifugation at 1000 g for 60 min. **Supporting Fig. S7:** Raman measurements were performed on multiple locations across the a) Au NPs (50 nm)@5kPSSH and b) Au NPs (70 nm)@12kPSSH/pSi hybrid structures under 2000 g for 30 min centrifugation conditions (optical microscopy images, laser spot size ∼1 μm). The spectra (c and d) consistently showed the characteristic vibrational modes of the PSSH ligands, with little variation in intensity or spectral features between spots. e) Comparison with spectra of the pure PSSH powders (5 kDa and 12 kDa) confirmed the assignment. No ligand signal was detected on the pSi substrate alone (no Au NPs). **Supporting Fig. S8:** Raman measurements on a polystyrene plate (450 μm, top row) and on multiple locations across an Au NPs (70 nm)@12kPSSH/pSi hybrid structure. Measurements were done on filled (golden) and on black pores (cf. Figure S7) with 633 nm or 785 nm excitation as indicated. For the polystyrene plate, 100x (NA = 0.25, red lines) and 10x objective (NA = 0.9, black lines) are compared, the measurements on pores were done with a 100x objective leading to a spot size of ∼1 μm in diameter. The measurements reveal that the black pores were clearly not empty but contained AuNPs (70 nm)@12kPSSH. In incompletely filled pores these cannot be discerned with optical microscopy. The measurements with 633 nm have a significant contribution of the Si phonon around 950 cm-1 from the substrate. **Supporting Fig. S9:** Raman measurements on multiple locations across an Au NPs (70 nm)@12kPSSH/pSi hybrid structure. Measurements were done on filled (golden) and on black areas (cf. Figure S7) with 633 nm or 785 nm excitation as indicated. The measurements were done with a 10x objective leading to a spot size of 3-4 μm in diameter, that covered more than a single pore. The measurements reveal that the black areas were clearly not empty but contained AuNPs (70 nm)@12kPSSH. In areas with incompletely filled pores these cannot be discerned with optical microscopy. **Supporting Fig. S10:** Ratio of the intensities (normalized by power density for the plasmonic samples (golden/black areas and pores) and by power and monomers for the polystyrene (PS) plates) with 633 nm excitation I(633 nm) and 785 nm excitation I(785 nm) for the different samples and regions. The spot size for the 10x objective was in the range 3-4 μm and for the 100x objective it was ∼1 μm. **Supporting Fig. S11:** Attractive van der Waals (vdW) interactions of two Au spheres (no coating, diameter d = 50 nm, Au–Au, blue line)) and of an Au sphere (d = 50 nm) and a silicon surface (Au–Si, orange dashed line) as a function of separation distance. Calculations were done as described by Bishop et al. [1] and Sun.[2] **Supporting Fig. S12:** Calculated free energy per unit area f(h) as a function of brush height h as described by Bishop et al.[1] The Kuhn length of polystyrene b = 1.8 nm, according numbers of (statistical) monomers N(12kPSSH) = 16 and N(5kPSSH) = 7, a grafting density of 0.5 nm-2 and T = 298 K were used. For the equilibrium height, experimental values (h0(5kPSSH) = 5 nm; h0(12kPSSH) = 8 nm) from Schulz et al. were used.[3] The interaction is dominated by the increasing osmotic pressure in the polymer shell upon compression and is always repulsive. It is also larger for 12kPSSH.